https://doi.org/10.5194/egusphere-2026-3174
Preprint. Discussion started: 21 July 2026

Overestimated organic condensation reveals an underperformance in estimation of ambient nanoparticle growth

Chuang Li[1], Runlong Cai[1,2,3], Zexin Chen[1], Gan Yang[1], Feilin Zhao[1], Yueyang Li[1], Jingyu An[4], Qiwen Sun[1], Sijia Yin[1], Shimeng Xu[1], Yiliang Liu[5], Douglas Worsnop[6], Lei Yao[1], Lin Wang[1,2,3,7]

[1]Shanghai Key Laboratory of Air Quality and Environmental Health, Department of Environmental Science & Engineering, Fudan University, Shanghai, 200438, China
[2]IRDR ICoE on Risk Interconnectivity and Governance on Weather/Climate Extremes Impact and Public Health, Fudan University, Shanghai, 200438, China
[3]National Observations and Research Station for Wetland Ecosystems of the Yangtze Estuary, Shanghai, China
[4]Key Laboratory of Formation and Prevention of Urban Air Pollution Complex, Ministry of Ecology and Environment, Shanghai Academy of Environmental Sciences, Shanghai, 200233, China
[5]Key Laboratory of Reservoir Aquatic Environment of CAS, Chongqing Institute of Green and Intelligent Technology, Chinese Academy of Sciences, Chongqing, 400714, China
[6]Aerodyne Research Inc., Billerica, MA 01821, USA
[7]Shanghai Institute of Pollution Control and Ecological Security, Shanghai, 200092, China

Correspondence to: Lin Wang (lin_wang@fudan.edu.cn)

Abstract

Atmospheric new particle formation (NPF) supplies up to half of global cloud condensation nuclei, yet the growth of sub-15 nm nanoparticles—the stage most vulnerable to scavenging—remains poorly constrained, largely because the volatility of oxygenated organic molecules (OOMs) is highly uncertain. Using a purpose-built laminar flow reactor that isolates particle–particle coagulation from OOM condensation, we show that six of seven widely used OOM volatility parameterizations substantially overestimate nanoparticle growth rates, with the largest bias under the high-NOx conditions. A recent parameterization constrained by ambient organic aerosol volatility reproduces our laboratory observations across diverse OOM precursors, seed sizes (3-5 nm), and NOx regimes. By applying this laboratory-validated framework to NPF events at Lake Tai, China, in summer 2023, OOM and H_2SO_4 condensation explain about 53% of the observed 3-15 nm growth rate, leaving a residual that persists even at the upper bound of measurement uncertainty. Together, our laboratory experiments and field observations provide strong evidence that particle coagulation and vapour condensation alone cannot account for ambient nanoparticle growth, revealing a clear gap in our understanding of this process. This gap may point to additional processes, not yet accounted for in current frameworks, that could contribute to nanoparticle growth in polluted atmospheres, or it may reflect uncertainties in other parameters.

https://doi.org/10.5194/egusphere-2026-3174
Preprint. Discussion started: 21 July 2026

1 Introduction

Formation of atmospheric new aerosol particles via gas-to-particle conversion is a key source of cloud condensation nuclei (CCN)(Dunne et al., 2016; Gordon et al., 2017), but only if nascent particles grow fast enough to escape the scavenging-prone sub-15 nm size range(Kuang et al., 2009). Condensation of sulfuric acid (H_2SO_4) and low-volatility oxygenated organic molecules (OOMs) are believed to driver this initial growth in the urban and forest atmosphere(Mohr et al., 2019; Qiao et al., 2021; Stolzenburg et al., 2025). Closure between simulation and observed growth rates (GRs) has been reported in selected atmospheric environments, including the boreal forest in Hyytiälä, Finland(Mohr et al., 2019), and roadside locations in Leipzig, Germany(Brean et al., 2024). However, broader observations enabled by multi-instrument OOM detection show that closure often fails across regions and seasons, with models under- or over-predicting 3-15 nm particle growth, for example in urban Beijing(Qiao et al., 2021) and again in Hyytiälä under different seasonal conditions(Stolzenburg et al., 2025). Such discrepancies, reflecting both model uncertainties and unrepresented growth mechanisms, bias estimates of global CCN and aerosol–cloud radiative effects and degrade air-quality forecasts (Carslaw et al., 2013; Gordon et al., 2017; Kulmala, 2025).

The main challenge in accurately quantifying the contribution of OOMs to nanoparticle growth lies in the uncertainties associated with their concentration and volatility(Mohr et al., 2019; Tröstl et al., 2016). While uncertainties in concentration measurements of OOMs by Chemical Ionization Mass Spectrometer (CIMS) can be generally constrained to ~50%, yielding growth-rate uncertainties below ~60% in typical urban or boreal forest environments, direct volatility measurements for individual OOMs remain extremely challenging owing to their very low vapor pressures and the lack of synthetic standards(Lopez-Hilfiker et al., 2016; Qiao et al., 2021; Sekimoto et al., 2017; Stolzenburg et al., 2025). As an alternative, typical volatility parameterizations may carry uncertainties of up to several orders of magnitude, potentially leading to errors by a factor of ~3-4 in simulated nanoparticle GRs(Donahue et al., 2011; Li et al., 2016; Mohr et al., 2019; Ren et al., 2022; Stolzenburg et al., 2018, 2025; Wang et al., 2020; Yang et al., 2023).

Given these large uncertainties in OOM volatility, it remains unclear whether coagulation and condensation alone can account for the observed growth of freshly formed nanoparticles, and how well current volatility parameterizations perform under different atmospheric regimes. Here, we present laminar flow reactor experiments that quantitatively resolve the respective contributions of particle-particle coagulation and OOM condensation to nanoparticle growth, thereby enabling a direct, controlled evaluation of widely used OOM volatility parameterizations against observed growth. We examine OOMs generated from α-pinene and toluene oxidation across a range of seed particle sizes (3-5 nm) and NOx conditions, and then apply the best-performing, laboratory-validated parameterization to NPF events observed at Lake Tai, China, in summer 2023 to assess the extent to which coagulation and vapour condensation can explain the growth of ambient 3–15 nm nanoparticles.

Methods

2.1 Laminar flow reactor and experimental setup.

https://doi.org/10.5194/egusphere-2026-3174
Preprint. Discussion started: 21 July 2026

A custom-designed laminar flow reactor was constructed to investigate the condensational growth of seed particles in the presence of OOMs, with three functional modules: seed-particle generation, OOM generation, and the main growth region (Fig. S1; full geometric and operational details in Supplementary Information, Text S1).

Self-charged polydisperse Ni-Cr seed nanoparticles were produced by resistive heating of a nichrome wire and classified to a monodisperse size distribution using a high-resolution half-mini differential mobility analyzer (half-mini-DMA) (Liu et al., 2020), yielding a size resolution of ~30 at a mobility diameter of 3.3 nm. The monodisperse outflow was split between a fast condensation particle counter (Fast CPC; Model 3650, Kanomax Inc., Japan) for online seed-number monitoring and the inlet of the laminar flow reactor.

OOMs were generated by hydroxyl radical (OH)-initiated oxidation of toluene or ozonolysis of α-pinene in a Potential Aerosol Mass (PAM) oxidation flow reactor (Aerodyne Research Inc.) operated at a residence time of ~52 s. For OH + toluene experiments, the PAM was run in the OFR254 mode, with OH generated in situ by 254 nm photolysis of O_3 in the presence of water vapor; for α-pinene experiments, the PAM operated as a dark ozonolysis reactor without UV. NO was added in selected experiments to produce controlled NOx levels, and 2.5 sccm of 10% CO was injected at the PAM outlet as an OH scavenger to terminate downstream oxidation. Relative humidity was maintained at 44–53%; experimental conditions are summarized in Table S1.

Seed nanoparticles and OOMs entered the growth region (200 cm long, 20 cm i.d.) through a coaxial inlet design (axial conical inlet for particles, annular inlet for OOMs) that promotes rapid radial mixing while preserving laminar flow ($Re < 200$). At a total flow of 21 L min^{-1}, the residence time was ~3 min. Nine axial sampling ports, distributed at 20 cm intervals starting 35 cm downstream of the OOM injection plane, enabled time-resolved measurements of particle size and number with a TSI® 1-nm SMPS (Model 3938E57), and of OOM concentrations with three online mass spectrometers (Vocus-PTR, iodide-CIMS, and nitrate-CIMS; Aerodyne Research Inc., USA and Tofwerk AG, Switzerland). A particle size magnifier (PSM; Model A10, Airmodus Inc., Finland) and a nano-SMPS (Model 3936, TSI Inc., USA) at the 180 s port verified the absence of new particle formation under condensation conditions.

2.2. Generation and quantification of citric acid and PEG-7 vapors.

Citric acid (saturation vapor pressure estimated by group contribution methods (Moller et al., 2008; Nannoolal et al., 2004) and validated against FIGAERO-iodide-CIMS measurements (Ren et al., 2022; Ye et al., 2019)) and PEG-7 (with a directly measured vapor pressure (Krieger et al., 2017)) were generated by passing zero-air over heated reservoirs (45–80 °C for citric acid; 52–85 °C for PEG-7). Citric acid was quantified with the nitrate-CIMS and PEG-7 with the iodide-CIMS, using liquid-injection calibrations (calibration factors: 1.35×10^{12} cm^{-3} for citric acid and 9.44×10^{11} cm^{-3} for PEG-7; Fig. S2).

2.3 Measurement and quantification of OOMs.

Gas-phase OOMs (defined as molecules containing at least one C, H, and O atom) were measured by three complementary mass spectrometers, all equipped with long time-of-flight analyzers (mass resolution 8,000–9,000 Th/Th). The Vocus-PTR

https://doi.org/10.5194/egusphere-2026-3174
Preprint. Discussion started: 21 July 2026

was calibrated using a multi-component gas-phase standard (Table S2), and sensitivities for non-calibrated OOMs were estimated from their proton-transfer reaction rate constants (Sekimoto et al., 2017) (Fig. S3). The iodide-CIMS followed the Lopez-Hilfiker et al. (Lopez-Hilfiker et al., 2016) calibration scheme, with declustering-voltage scans converting iodide–OOM adduct stabilities (dV_{50}) into compound-specific sensitivities (Table S3 and Fig. S4). The nitrate-CIMS was calibrated assuming OOMs ionize at the H_2SO_4 collision limit (Tröstl et al., 2016; Yao et al., 2018), with mass-dependent transmission corrections (Heinritzi et al., 2016). Estimated systematic uncertainties are ±20% (Vocus-PTR, calibrated species), ~60% (iodide-CIMS, OOM mixtures), and ±50% (nitrate-CIMS).

For OOMs detected by multiple instruments, concentrations were assigned according to the oxygen number (n_o): nitrate-CIMS for $n_O \geq 6$; iodide-CIMS for $n_O \leq 3$ (vs. nitrate-CIMS) or $n_O \geq 4$ (vs. Vocus-PTR); Vocus-PTR for $n_O \leq 1$. For overlapping intermediate ranges (n_O = 4–5 between iodide and nitrate; n_O = 2–3 between iodide and Vocus-PTR), the higher of the two estimates was used (Figs. S5 and S6). Real-time axial concentration profiles of each OOM along the flow reactor were derived from regression of measured concentrations against residence time at the nine sampling ports (Fig. S7) and used as input to the growth model. See details in Supplementary Information, Text S2.

2.4 Volatility parameterization and growth simulation.

Saturation concentrations C^* of individual OOMs were estimated from their molecular formulas using published parameterizations; the Zhang et al. (2026) scheme is given by

$$log_{10}C^*(300K) = (25 - n_C)b_C - (n_O - 3n_N)b_O - 2\frac{(n_O - 3n_N)n_C}{(n_C + n_O - 3n_N)}b_{CO} - n_N b_N, (1)$$

b_C=0.493, b_O=1.392, b_{CO}=-0.532, and b_N=2.402 from Zhang et al. (2026). C^* was corrected to ambient temperature using a vaporization enthalpy $\Delta H_{vap} = -5.7 \log_{10}C^*(300\ K) + 129$ kJ mol^{-1} (Supplementary Information, Text S3).

Nanoparticle growth was simulated following the Stolzenburg et al. (2022) monodisperse VBS framework, which solves the coupled mass-transfer equations for OOM condensation across volatility bins together with kinetically limited H_2SO_4 condensation. Particle-phase activity, Kelvin correction, and hard-sphere collision kernels are described in Supplementary Information, Text S4. H_2SO_4 was measured by the nitrate-CIMS (calibration factor 8.03 × 10^9 cm^{-3}).

2.5 Field measurements.

A field campaign was conducted from 4 July to 20 September 2023 at the National Field Observation and Research Station for the Lake Ecosystem of Lake Tai (31°42′N, 120°22′E; ~5 m above sea level), a suburban site in Jiangsu Province, China, influenced by both anthropogenic and biogenic emissions. PNSDs from 1.2 to 700 nm were measured in parallel by a TSI® 1-nm SMPS, a TSI® Long-SMPS, and an Airmodus® PSM at 1–4 min resolution. Twelve NPF events were observed, four of which were selected for detailed analysis based on moderate background condensation sinks and smooth growth behavior. Gas-phase OOMs at the site were measured using the same nitrate-CIMS, iodide-CIMS, and Vocus-PTR as in the laboratory,

https://doi.org/10.5194/egusphere-2026-3174
Preprint. Discussion started: 21 July 2026

with sampling configurations detailed in Supplementary Information, Text S5.

3 Results and discussion

3.1 Condensation-driven growth of nanoparticles

A laminar flow reactor (Fig. S1a) was developed to investigate the growth of nanoparticles through particle-particle coagulation and condensation of organics. This laminar flow reactor sets the beginning of exposure upon the particle-vapor mixing and a residence time of 180 s at the 9th axial sampling point with a total flow rate of 21 L min^{-1}. Self-charged Ni-Cr oxide nanoparticles were generated by resistive heating of a nichrome wire, classified to a monodisperse diameter using a custom-made half-mini-DMA with peak number concentrations of (1.5-2.0) × 10^5 cm^{-3} (dN/dlogD_p, cm^{-3}), and then introduced into the laminar flow reactor(Liu et al., 2021)(Supplementary Information, Text S1 and Fig. S8). The evolution of number concentrations and mode diameters of charged Ni-Cr oxide nanoparticles was measured by a TSI® 1-nm SMPS at nine axial sampling points along the growth region. Owing to the limited resolution of the 1-nm SMPS (~7 at 3.3 nm), the geometric standard deviations (GSDs) of measured particle number size distributions (PNSDs) ($GSD_{1\text{-nm SMPS}} < 1.08$) were slightly larger than the true values obtained from the half-mini-DMA ($GSD_{\text{half-mini-DMA}} = 1.01$); the mode diameters, however, were unaffected (Fig. S8). No measurable increase in mode diameter was observed over the 180 s residence time (Fig. 1a), consistent with the < 0.1 nm increase predicted by inter-particle coagulation simulations (Cai et al., 2020). The simulation also predicts a coagulation-driven number loss rate of 0.01% s^{-1}; subtracted from the observed number loss rate of 0.11% s^{-1}, this yields a wall-loss rate of 0.10% s^{-1} for 3.3-nm Ni-Cr oxide nanoparticles.

The monodisperse Ni-Cr oxide nanoparticles were then exposed to two condensable vapors with well-characterized volatilities in two separate sets of experiments: polyethylene glycol-7 (PEG-7), whose saturation vapor pressure has been experimentally measured (Krieger et al., 2017), and citric acid, whose saturation vapor pressure was estimated by group contribution methods (Moller et al., 2008; Nannoolal et al., 2004) and validated against FIGAERO-iodide-CIMS measurements (Ren et al., 2022; Ye et al., 2019). Gaseous citric acid concentrations in four experiments — including a reference experiment (Exp. 1) in which no citric acid was introduced (Fig. 1b) — were measured at the 180 s sampling port by a nitrate ion-based chemical ionization mass spectrometer (nitrate-CIMS); concentrations along the reactor axis (Fig. 1c) were inferred from the experimentally determined first-order wall-loss rate constant of citric acid (Fig. S9). Correspondingly, the mode diameter of the seed nanoparticles increased from 3.3 nm to 3.4, 3.6, and 3.8 nm under three increasing citric acid concentrations (Fig. 1d). Parallel experiments with PEG-7 (Exp. 5–8 in Fig. S10) produced comparable concentration-dependent growth.

We then simulated nanoparticle growth from the measured saturation vapor pressures and axial concentration profiles of citric acid or PEG-7 (Supplementary Information, Text S6 and Fig. S9). Fig. 1e compares the measured GRs with simulated values across the concentration ranges examined. A strong correlation between measured and simulated GRs was observed, with data points generally scattered within a factor of 1.5 along the 1:1 line, confirming that our growth model accurately reproduces condensation-driven nanoparticle growth.

https://doi.org/10.5194/egusphere-2026-3174
Preprint. Discussion started: 21 July 2026

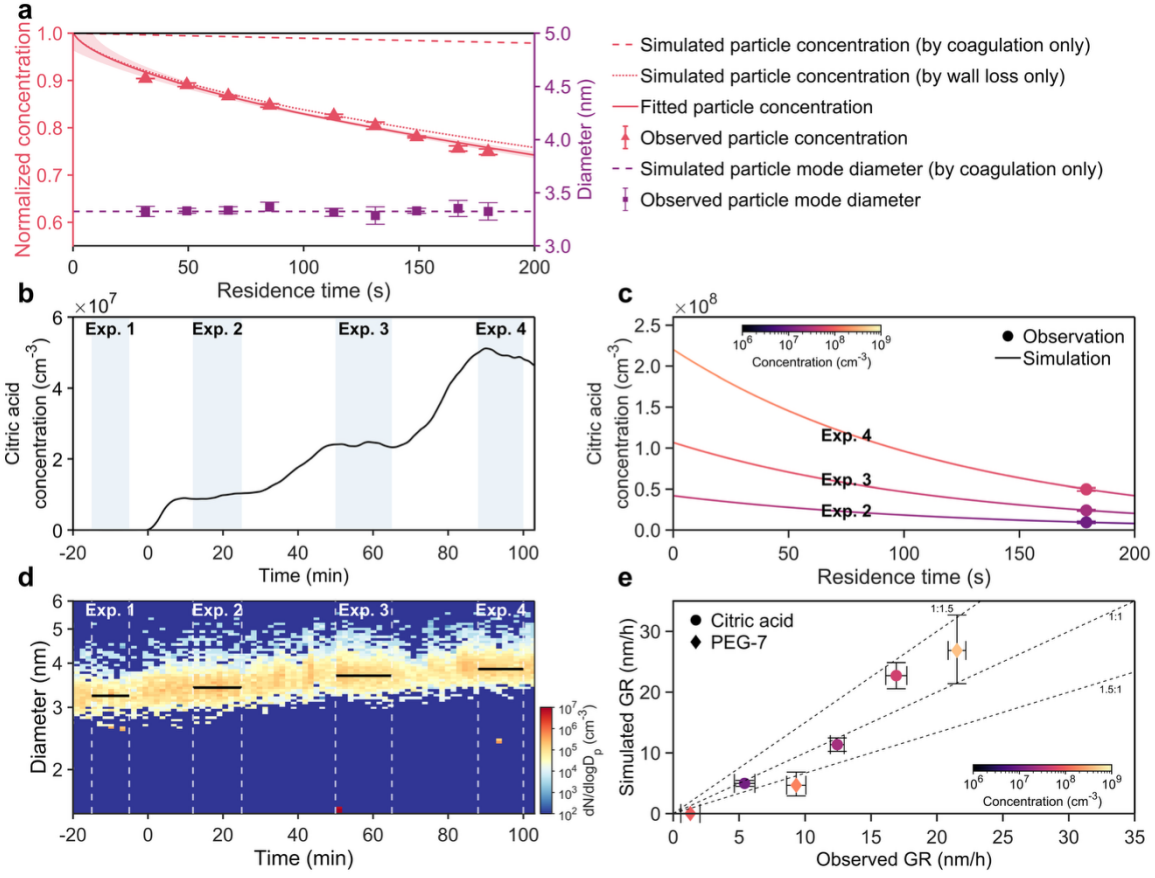

Figure 1. Coagulation- and condensation-driven growth of monodisperse Ni-Cr oxide nanoparticles in a laminar flow reactor. (a) Normalized number concentrations (red triangles) and mode diameters (purple squares) of Ni-Cr oxide nanoparticles at nine sampling points. The dashed purple line and dashed red line illustrate theoretical evolutions of the particle mode diameter and number, respectively, due to coagulation. The solid red line represents the observed decay of Ni-Cr oxide nanoparticle concentration, which, together with the red dashed line, gives the red dotted line indicating wall losses of Ni-Cr oxide nanoparticles. (b) Citric acid concentrations measured by nitrate-CIMS at a fixed residence time of 180 s in the laminar flow reactor; light blue shaded intervals denote Exp. 1-4, among which the citric acid exposure was zero in Exp. 1. (c) Observed citric acid concentrations at a residence time of 180 s for Exp. 2-4. Colored lines represent back-calculated concentrations of citric acid with incorporation of wall loss using the loss-rate coefficient of citric acid (refer to Fig. S1). (d) Particle number size distributions (PNSDs) of Ni-Cr oxide nanoparticles during Exp. 1-4. Vertical dashed white lines mark experimental boundaries, and horizontal black lines indicate the mean mode particle diameter in each experiment. (e) Comparison of experimentally measured particle GRs and simulated ones when exposing nanoparticles to citric acid or PEG-7. Circles and diamonds represent citric acid and PEG-7 experiments, respectively, under varying concentrations. The dashed lines depict 1:1, 1:1.5, and 1.5:1 reference ratios, and error bars for a datapoint indicate one standard deviation of the measurement mean.

3.2 Evaluation of volatility parameterizations

Next, we investigated OOM-mixture-driven growth of monodisperse Ni-Cr oxide nanoparticles using OOMs generated from the oxidation of toluene or α-pinene under high and low NOx in the laminar flow reactor (Table S1). As an illustrative example, 3.3-nm Ni-Cr oxide nanoparticles were exposed to OOMs from α-pinene ozonolysis under low-NOx conditions; the OOM

https://doi.org/10.5194/egusphere-2026-3174
Preprint. Discussion started: 21 July 2026

abundances were controlled by varying the α-pinene concentration. Four quasi-steady sampling periods (Exp. 9-12) captured successive growth stages (Fig. 2a, b). Note that the residual OOMs detected in Exp. 9 (Fig. 2a) before O_3 introduction did not produce measurable particle growth; the particle size measured at the 131 s sampling port in Exp. 9 was therefore used as the initial particle size (3.3 nm) at t = 0 s (Fig. 2c). In the other three experiments (Exp. 10-12), the mode diameter of the seed nanoparticles increased from 3.3 nm to 3.5, 3.7, and 3.9 nm (Fig. 2c), corresponding to GRs of 5.5, 11.0, and 16.5 nm h^{-1}, respectively.

Fig. 2d presents a mass defect plot of all detected OOMs. Species were measured by three complementary instruments: a Vocus proton-transfer-reaction mass spectrometer (Vocus-PTR), an iodide-ion-based chemical ionization mass spectrometer (iodide-CIMS), and a nitrate-ion-based chemical ionization mass spectrometer (nitrate-CIMS), with many species detected by two or all three instruments. Concentrations of individual OOMs were quantified by instrument-specific calibrations (see Sect. 2.3). Note that identical molecular formulas across instruments do not necessarily correspond to identical structures, given the diversity of possible isomers.

For OOMs detected by both iodide-CIMS and nitrate-CIMS**,** the two estimates agreed within an order of magnitude only for species with oxygen number (n_O) = 4–5, while diverging systematically at lower or higher oxygen numbers (Fig. S5*)*. Because CIMS sensitivity depends strongly on the oxygen number (n_O) of OOMs (Riva et al., 2019), formulas with $n_O \leq 3$ were quantified by iodide-CIMS, those with $n_O \geq 6$ by nitrate-CIMS, and those with n_O = 4–5 were assigned the higher of the two estimates. For OOMs detected by both Vocus-PTR and iodide-CIMS, the two estimates showed larger discrepancies than for the iodide-CIMS / nitrate-CIMS pair (Fig. S6), reflecting fragmentation of multifunctional OOMs in Vocus-PTR (Li et al., 2022; Zhang et al., 2025). Following the same logic, formulas with n_O = 0 or 1 were quantified by Vocus-PTR, those with $n_O \geq 4$ by iodide-CIMS, and those with n_O = 2 or 3 were assigned the higher of the two estimates. For OOMs detected by both Vocus-PTR and nitrate-CIMS, the nitrate-CIMS estimate was used. For species detected by all three instruments, the iodide-CIMS / nitrate-CIMS rule was applied and the Vocus-PTR estimate was discarded. Importantly, the OOMs with the largest discrepancies ($n_O < 4$) are sufficiently volatile that they do not contribute to sub-15 nm particle growth owing to the Kelvin effect (Fig. S11); their impact on simulated GRs is therefore limited.

We then applied seven volatility parameterizations to the OOMs detected in Exp. 12 to calculate their saturation vapor concentrations, yielding seven Volatility Basis Set (VBS) representations spanning ultra-low-volatility, extremely low-volatility, low-volatility, semi-volatile, intermediate-volatility, and volatile organic compounds (ULVOC, ELVOC, LVOC, SVOC, IVOC, and VOC) (Fig. 2e and Fig. S12). Although all seven schemes spanned the full ULVOC-VOC range, they showed systematic offsets in their assigned $\log_{10}C^*$ values, leading to markedly different volatility distributions. The (Zhang et al., 2026) scheme is shifted most strongly toward higher volatility, assigning 91% of OOMs to VOCs and 8% to IVOCs, with only 0.67% combined in ULVOC, ELVOC, and LVOC (Fig. 2a).

https://doi.org/10.5194/egusphere-2026-3174
Preprint. Discussion started: 21 July 2026

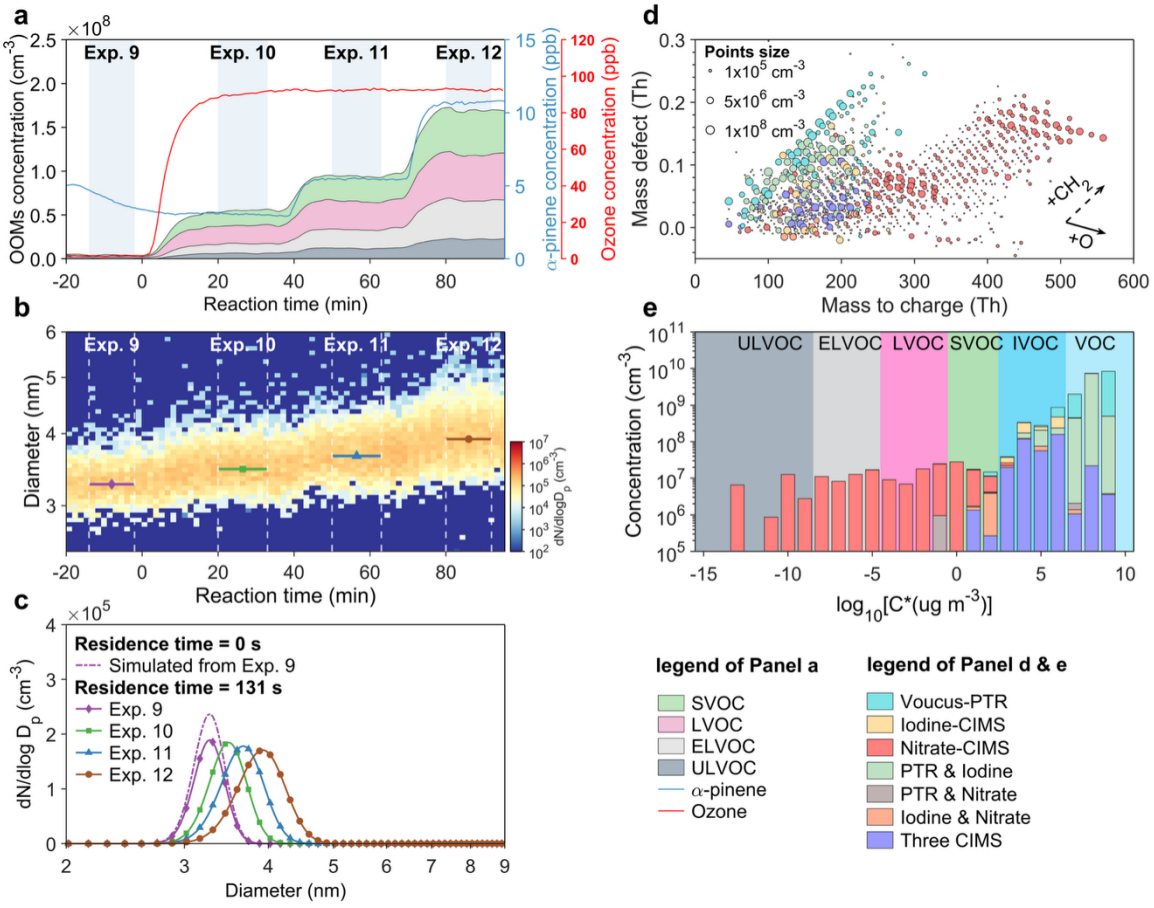

Figure 2. Particle growth driven by condensation of OOMs formed from α-pinene + O_3 under low NOx conditions. (a) Profiles of gas-phase precursors and total concentrations of SVOC, LVOC, ELVOC, and ULVOC during four experiment periods (Exp. 9-12) as highlighted in shaded regions. (b) PNSDs of Ni-Cr oxide nanoparticles during Exp. 9-12. Vertical dashed white lines mark experimental boundaries, and horizontal-colored lines indicate the mean mode particle diameter in each experiment. (c) PNSDs in Exp. 9-12. The dashed line represents the simulated size distribution at a residence time of 0 s based on Exp. 9. The solid lines represent measured PNSDs at a residence time of 131 s for Exp. 9-12, illustrating particle growth resulting from condensation of varying concentrations of OOMs. (d) Mass defect plot for all assigned OOMs in Exp. 12. Marker size scales with OOMs' concentration. Marker color indicates which of the three CIMS (Vocus-PTR, iodide-CIMS, nitrate-CIMS) detected the OOMs, including overlaps, following the color scheme in the bottom right panel. (e) OOM concentration as a function of effective saturation concentration ($\log_{10}C^*$), grouped into volatility classes (ULVOC→VOC). Volatility estimates of OOMs are derived using the parameterization of Zhang et al. (2026). Bars show the concentrations of OOMs detected by at least one of three CIMS, following the color scheme in the bottom-right panel. Please refer to the main text for quantification rules.

We then compared the measured PNSDs for Exp. 12 with those simulated from the measured concentration profiles in the flow reactor (Fig. S12) and the parameterized volatilities (Fig. 2e) of individual OOMs. All seven simulated PNSDs overestimated the observed particle growth to varying degrees (Fig. 3a): the Zhang et al. (2026) parameterization showed the smallest overestimation, followed by Li et al. (2016), Mohr et al. (2019), and Dada et al. (2023). When nanoparticles were

https://doi.org/10.5194/egusphere-2026-3174
Preprint. Discussion started: 21 July 2026

exposed to OOMs formed from α-pinene + O_3 under high-NOx conditions (Exp. 13–16; Fig. S13), the Li et al. (2016), Mohr et al. (2019), and Dada et al. (2023) parameterizations exhibited substantially larger overestimations than under low-NOx conditions (Fig. 3b), whereas the Zhang et al. (2026) parameterization continued to perform best. This is consistent with the better agreement between the Zhang et al. (2026) parameterization and CHON-compound volatilities tabulated in the National Cancer Institute (NCI) open database.

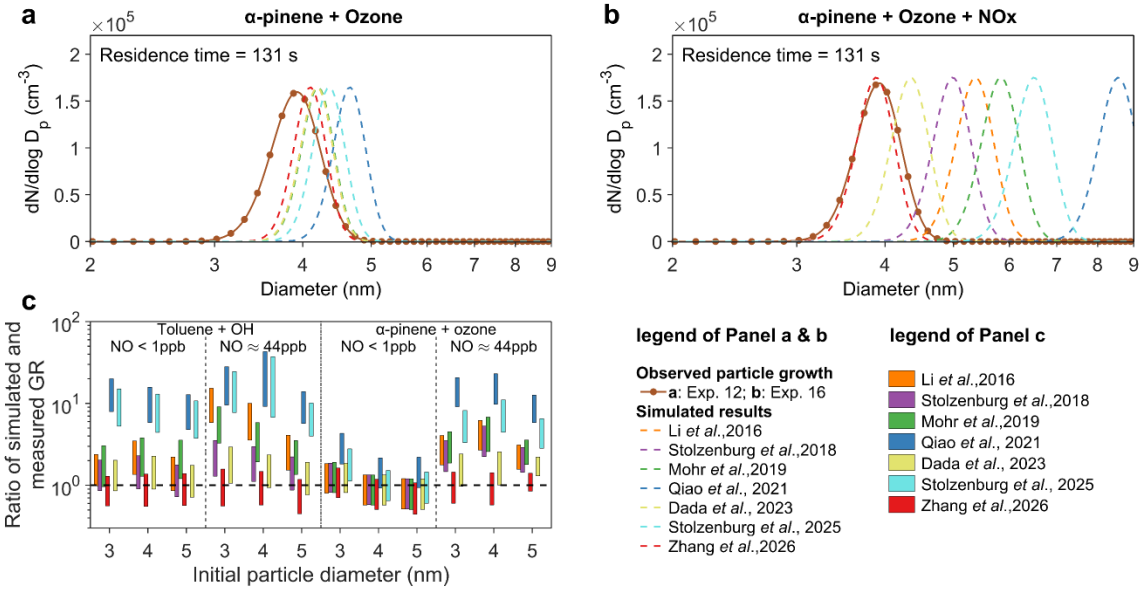

Figure 3. Comparison of observed and simulated growth of Ni-Cr oxide nanoparticles when exposed to OOMs. (a) Comparison of observed PNSDs (solid line) after exposing Ni-Cr oxide nanoparticles to OOMs formed from α-pinene + O_3 oxidation under low NOx conditions (Exp. 12), with simulated ones (dashed lines) using seven VBSs. (b) Comparison of observed PNSD (solid line) after exposing Ni-Cr oxide nanoparticles to OOMs formed from α-pinene + O_3 oxidation under high NOx conditions (Exp. 16), with simulated ones (dashed lines) using seven VBS schemes. (c) Ratios of simulated to measured GRs as a function of initial mode diameter under four OOM source scenarios: toluene + OH or α-pinene + O_3 with low (NO < 1 ppb) or high (NO ≈ 44 ppb) NOx conditions. Colors and symbols indicate different GR simulation methods. The upper and lower bounds of the columns represent the simulation uncertainties associated with a +50%/−50% error in OOMs' concentrations. The dashed line represents the 1:1 reference.

To assess the generality of these findings, we examined experiments spanning different seed nanoparticle diameters (3-5 nm) and OOM types from either toluene + OH or α-pinene + O_3 under low- or high-NOx conditions (Exp. 9–56 in Table S1; Figs. 2a-d, Figs. S13-S15 for growth experiments and Figs. 2e, Figs. S16–S18 for volatility parameterizations). The simulated-to-measured GR ratios for all conditions are summarized in Fig. 3c. The Stolzenburg et al. (2025) and Qiao et al. (2021) schemes systematically overpredicted growth across a wide range of conditions. Notably, both schemes were developed from volatility frameworks largely constrained by biogenic volatile organic compounds (BVOC) oxidation chemistry: Stolzenburg et al. (2025) refined the formulation using BVOC autoxidation products, whereas Qiao et al. (2021) built on the revision by Mohr et al. (2019), which was derived from HOM measurements of α-pinene oxidation. By contrast, the Li et al., (2016), Mohr et al., (2019), Stolzenburg (2018), and Dada et al., (2023) schemes reproduced the measured GRs under low-NOx conditions but

https://doi.org/10.5194/egusphere-2026-3174
Preprint. Discussion started: 21 July 2026

overpredicted growth under high-NOx conditions, particularly for OOMs from toluene + OH oxidation, which are more representative of urban atmospheres. Together, these results suggest that BVOC-derived volatility frameworks describe OOM-driven growth reasonably well in relatively clean, low-NOx regimes (e.g., α-pinene + O_3 oxidation). They are less transferable to polluted, high-NOx environments, where anthropogenic precursors and intensified NOx pathways likely generate OOM populations with distinct functionality, volatility, and condensational behavior.

3.3 Ambient nanoparticle growth

We analyzed field NPF events at Lake Tai, China in summer 2023, focusing on gaseous molecular compositions and PNSDs (see Sect. 2.5). High-resolution mass spectrometry measurements from Vocus-PTR, iodide-CIMS, and nitrate-CIMS revealed a wide molecular diversity of ambient gaseous OOMs, with each instrument capturing OOMs of different volatility and oxidation states, as illustrated by an example on 30 July 2023 (Fig. 4a, b). The volatility classification of ambient OOMs (Fig. 4b), based on estimated saturation concentrations (C*) using the Zhang et al. (2026) scheme, indicates that a substantial fraction (0.39%) of detected species fell into the ELVOC and LVOC classes.

Fig. 4c presents a comparison of observed and simulated growth trajectories of newly formed nanoparticles following their formation on 30 July 2023. The growth of 3-nm nanoparticles was simulated as the sum of particle coagulation, H_2SO_4 condensation, and OOM condensation using OOMs volatilities from seven parameterization schemes. Among all schemes, Zhang et al. (2026) was the only one that underpredicted particle growth, whereas the others overpredicted growth to varying degrees. Together with our laboratory results, this pattern suggests that commonly used parameterizations assign OOMs volatilities that are too low, thereby overstating their condensational contribution to early nanoparticle growth. For example, the calculated GRs were larger than the measured ones in Hyytiälä, Finland, which was previously explained by evaporation of particulate matter but could stem from the parametrization itself(Stolzenburg et al., 2025). Fig. 4d focuses on the comparison between the observed nanoparticle mode diameter evolution and the Zhang et al. (2026) scheme's prediction. Notably, the simulated mode diameters remained below the observed values and explained only 53% of the 3-15 nm nanoparticle growth rate. An uncertainty envelope (-50%/+50%) was applied to OOM concentrations, yielding an uncertainty of approximately -45% to +50% for the condensation-driven growth. Even at the upper bound of this uncertainty range, the simulated 3-15nm growth rate still left a residual ~14% gap relative to the observations. Beyond this single event, Fig. 4e presents the campaign-average behavior across four NPF events. The simulations systematically underestimated nanoparticle growth, particularly in the sub-15 nm size range, pointing to additional growth mechanisms.

https://doi.org/10.5194/egusphere-2026-3174
Preprint. Discussion started: 21 July 2026

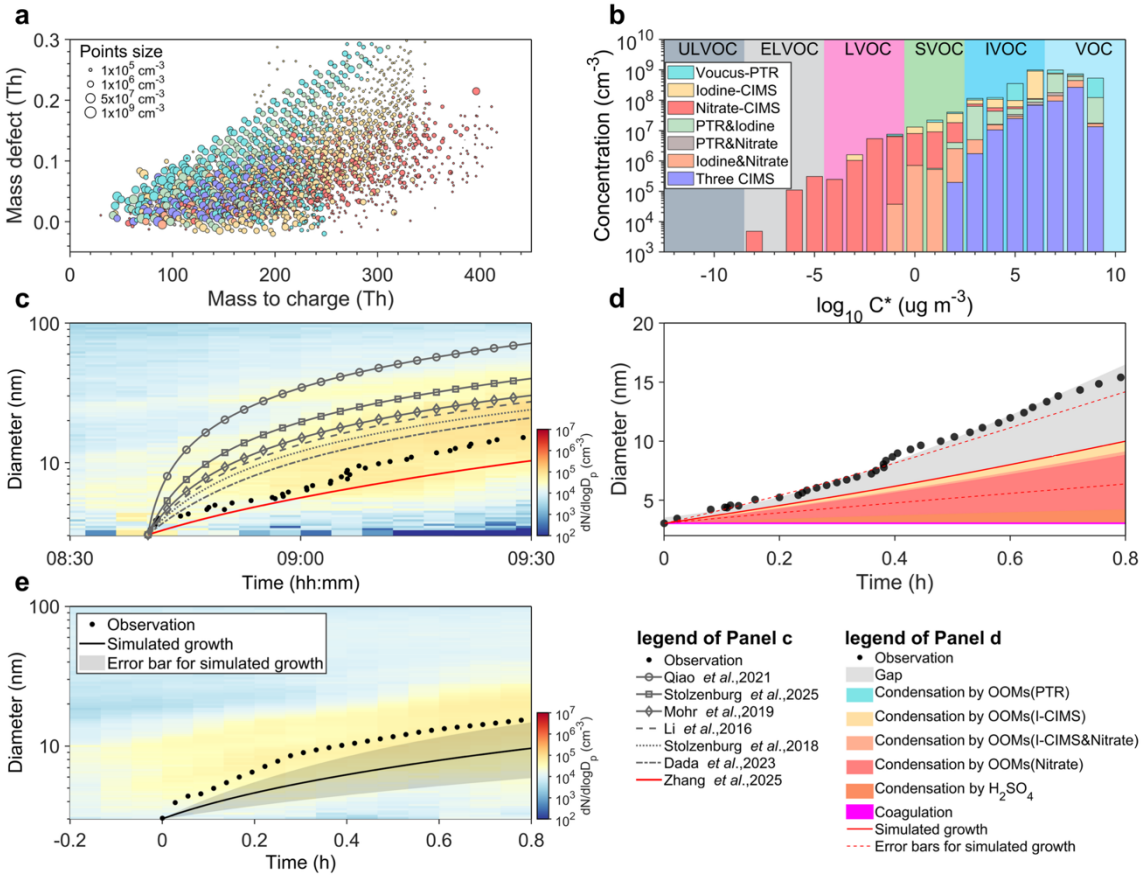

Figure 4. Characterization of ambient OOMs and their contribution to nanoparticle growth. (a) Mass defect plot of ambient OOMs detected at Lake Tai on 30th July, 2023, using three CIMS; Marker color follows the legend in panel b, Marker size denotes the relative ion signal intensity. (b) Volatility distribution of ambient OOMs classified into ULVOC, ELVOC, LVOC, SVOC, IVOC, and VOC, based on estimated saturation concentrations. Bars show the concentrations of OOMs detected by at least one of the three CIMS. Please refer to the main text for quantification rules. (c) Evolution of nanoparticle mode diameter during an ambient NPF event in Lake Tai on 30th July, 2023, overlaid on the PNSDs (dN/dlogDp, cm^{-3}). Black dots represent the observed particle mode diameter. Modeled growth curves based on different volatility parameterization methods (Qiao et al. (2021), Mohr et al. (2019), Li et al. (2016), Stolzenburg et al. (2018& 2025), Dada et al. (2023), and Zhang et al. (2026)) are shown for comparison. (d) Decomposition of the observed ambient nanoparticle growth into contributions from OOM condensation, H_2SO_4 condensation, and coagulation of nanoparticles for a NPF event in Lake Tai on 30th July, 2023. Black circles denote the observed mode diameter. The colored stacked areas show growth driven by coagulation of nanoparticles, condensation of H_2SO_4, and condensation of OOMs, respectively. The solid red line represents the simulated particle mode diameter. The grey shaded area ("Gap") indicates the unexplained growth not captured by these processes. The dashed red line marks the higher and lower uncertainty bounds of the simulated particle mode diameter from uncertainties in OOMs' concentrations. (e) Average PNSDs of four NPF events during the field campaign, with the particle mode diameter of 3 nm in all events serving as the starting point. Black dots represent the observed particle mode diameter. The black line gives the simulated growth based on particles coagulation and H_2SO_4 and OOMs condensation using the laboratory-validated volatility

https://doi.org/10.5194/egusphere-2026-3174
Preprint. Discussion started: 21 July 2026

parameterization (Zhang et al., 2026), and black shadow denotes the uncertainty of the simulated diameter propagated from uncertainties in OOMs' concentrations.

4 Conclusions and outlook

This study tackles a long-standing question: whether condensation of H_2SO_4 and OOMs alone can account for the rapid growth of freshly nucleated nanoparticles. Using a laminar flow reactor that cleanly separates particle–particle coagulation from OOM condensation, we benchmarked seven widely used volatility parameterizations directly against observed growth. Across diverse OOM precursors (α-pinene and toluene), seed nanoparticle sizes (3-5 nm), and NOx regimes, six of the seven overestimated nanoparticle growth-most severely under the high-NOx conditions typical of polluted urban air-whereas only a parameterization constrained by ambient organic-aerosol volatility (Zhang et al., 2026) reproduced our observations.

The nanoparticle growth is overestimated because existing parameterizations underestimate the volatility of OOMs formed under high-NOx conditions and thus overstate the fraction that can condense onto growing nanoparticles. Most existing parameterizations were derived from, or tuned to, biogenic, low-NOx oxidation systems dominated by CHO compounds, and they tend to assign lower volatilities to the OOM populations generated under high-NOx, anthropogenically influenced conditions. Such conditions favour nitrogen-containing products (e.g., organonitrates) and fragmentation pathways that shift the volatility distribution toward higher volatility, so that schemes calibrated on biogenic chemistry overstate the condensation flux of organics. This interpretation is supported by the fact that the Zhang et al. (2026) parameterization, which is constrained by directly measured volatilities of ambient urban and suburban particulate OOMs, alone reproduces our observations. The fundamental insight is therefore not that any individual parameterization is inherently deficient, but that the volatility-composition relationship is sensitive to the chemical regime in which it is calibrated, particularly the prevailing NOx level.

Applying this laboratory-validated Zhang et al. 2026 framework to NPF events at Lake Tai in summer 2023, OOM and H_2SO_4 condensation together explained about 53% of the observed 3-15 nm growth rate, with a residual that persisted even at the upper bound of measurement uncertainty (a ~14% gap). This gap may point to additional processes, not yet accounted for in current frameworks, that could contribute to nanoparticle growth in polluted atmospheres, or it may reflect uncertainties in other parameters.

Heterogeneous chemistry at nanoparticle surfaces offers one: by converting relatively volatile gases into lower-volatility products that overcome the Kelvin barrier, it can drive growth even from highly volatile vapors (Wang et al., 2010). Incorporating heterogeneous reactions of isoprene-derived epoxydiols (IEPOX)/methacrylic acid epoxide (IMAE), nitrogen oxides, and glyoxal/methylglyoxal substantially reduced this gap and brought the simulations toward the measurements (Fig. S19), indicating that gas–particle heterogeneous chemistry could be one potentially important yet currently unparameterized candidate contributor that merits dedicated investigation (see Supplementary Information, Text S7 and S8 for details).

On the other hand, several uncertainties may nonetheless bias the predicted growth rates, including those in OOM quantification (from instrument calibration and ionization efficiency), the well-mixed-particle assumption of the growth model, and its incomplete treatment of particle-phase reactions and chemical aging. Our conclusions also rest on a single campaign

https://doi.org/10.5194/egusphere-2026-3174
Preprint. Discussion started: 21 July 2026

with a limited number of events, precluding generalization across seasons, source regimes, or meteorological conditions. These caveats notwithstanding, the results caution against applying volatility frameworks calibrated largely on biogenic, clean-environment chemistry to polluted, high-NOx atmospheres, where such frameworks may overstate the organic contribution to early growth and thereby bias estimates of CCN abundance and aerosol–cloud radiative forcing. Establishing a transferable, mechanistically complete description of nanoparticle growth will require extending these co-evaluated laboratory and field analyses to diverse polluted atmospheres, alongside direct volatility measurements and explicit kinetic treatment of particle-phase heterogeneous reactions.

Code and data availability

The data underlying all figures will be made publicly available upon acceptance, and the DOI will be provided at that time.

Supplement link

The supplement related to this article is available online at xx

Author contributions

LW conceived and led the study; CL and LW developed the methodology; CL, FZ, YYL, and YLL performed the laboratory experiments; CL, GY, SY, and YL performed the field measurements; CL and Z-XC analyzed the field data; CL, RC, Z-XC, and JA performed the simulations; CL and LW wrote the manuscript draft; all coauthors reviewed and edited the manuscript.

Competing interests

The authors declare no competing interests.

Disclaimer

Publisher's note: Copernicus Publications remains neutral with regard to jurisdictional claims made in the text, published maps, institutional affiliations, or any other geographical representation in this paper. While Copernicus Publications makes every effort to include appropriate place names, the final responsibility lies with the authors. Views expressed in the text are those of the authors and do not necessarily reflect the views of the publisher.

https://doi.org/10.5194/egusphere-2026-3174
Preprint. Discussion started: 21 July 2026

Acknowledgements

The authors gratefully acknowledge the National Field Observation and Research Station for the Lake Ecosystem of Lake Tai for providing access to the observation site and supporting infrastructure during the 2023 summer field campaign.

Financial support

This research has been supported by Jing-Jin-Ji Regional Integrated Environmental Improvement-National Science and Technology Major Project (2026ZD1209900) and National natural science foundation of China (22127811 and 21925601).

References

Brean, J., Rowell, A., Beddows, D. C. S., Weinhold, K., Mettke, P., Merkel, M., Tuch, T., Rissanen, M., Maso, M. D., Kumar, A., Barua, S., Iyer, S., Karppinen, A., Wiedensohler, A., Shi, Z., and Harrison, R. M.: Road Traffic Emissions Lead to Much Enhanced New Particle Formation through Increased Growth Rates, Environ. Sci. Technol., 58, 10664–10674, https://doi.org/10.1021/acs.est.3c10526, 2024.

Cai, R., Li, C., He, X.-C., Deng, C., Lu, Y., Yin, R., Yan, C., Wang, L., Jiang, J., Kulmala, M., and Kangasluoma, J.: Impacts of coagulation on the appearance time method for new particle growth rate evaluation and their corrections, Atmos. Chem. Phys., 21, 2287–2304, https://doi.org/10.5194/acp-21-2287-2021, 2020.

Carslaw, K. S., Lee, L. A., Reddington, C. L., Pringle, K. J., Rap, A., Forster, P. M., Mann, G. W., Spracklen, D. V., Woodhouse, M. T., Regayre, L. A., and Pierce, J. R.: Large contribution of natural aerosols to uncertainty in indirect forcing, Nature, 503, 67–71, https://doi.org/10.1038/nature12674, 2013.

Donahue, N. M., Epstein, S. A., Pandis, S. N., and Robinson, A. L.: A two-dimensional volatility basis set: 1. organic-aerosol mixing thermodynamics, Atmos. Chem. Phys., 11, 3303–3318, https://doi.org/10.5194/acp-11-3303-2011, 2011.

Dunne, E. M., Gordon, H., Kürten, A., Almeida, J., Duplissy, J., Williamson, C., Ortega, I. K., Pringle, K. J., Adamov, A., Baltensperger, U., Barmet, P., Benduhn, F., Bianchi, F., Breitenlechner, M., Clarke, A., Curtius, J., Dommen, J., Donahue, N. M., Ehrhart, S., Flagan, R. C., Franchin, A., Guida, R., Hakala, J., Hansel, A., Heinritzi, M., Jokinen, T., Kangasluoma, J., Kirkby, J., Kulmala, M., Kupc, A., Lawler, M. J., Lehtipalo, K., Makhmutov, V., Mann, G., Mathot, S., Merikanto, J., Miettinen, P., Nenes, A., Onnela, A., Rap, A., Reddington, C. L. S., Riccobono, F., Richards, N. A. D., Rissanen, M. P., Rondo, L., Sarnela, N., Schobesberger, S., Sengupta, K., Simon, M., Sipilä, M., Smith, J. N., Stozkhov, Y., Tomé, A., Tröstl, J., Wagner, P. E., Wimmer, D., Winkler, P. M., Worsnop, D. R., and Carslaw, K. S.: Global atmospheric particle formation from CERN CLOUD measurements, Science, 354, 1119–1124, https://doi.org/10.1126/science.aaf2649, 2016.

Gordon, H., Kirkby, J., Baltensperger, U., Bianchi, F., Breitenlechner, M., Curtius, J., Dias, A., Dommen, J., Donahue, N. M., Dunne, E. M., Duplissy, J., Ehrhart, S., Flagan, R. C., Frege, C., Fuchs, C., Hansel, A., Hoyle, C. R., Kulmala, M., Kürten, A., Lehtipalo, K., Makhmutov, V., Molteni, U., Rissanen, M. P., Stozkhov, Y., Tröstl, J., Tsagkogeorgas, G., Wagner, R.,

https://doi.org/10.5194/egusphere-2026-3174
Preprint. Discussion started: 21 July 2026

Williamson, C., Wimmer, D., Winkler, P. M., Yan, C., and Carslaw, K. S.: Causes and importance of new particle formation in the present-day and preindustrial atmospheres, J. Geophys. Res.: Atmos., 122, 8739–8760, https://doi.org/10.1002/2017jd026844, 2017.

Heinritzi, M., Simon, M., Steiner, G., Wagner, A. C., Kürten, A., Hansel, A., and Curtius, J.: Characterization of the mass-dependent transmission efficiency of a CIMS, Atmos. Meas. Tech., 9, 1449–1460, https://doi.org/10.5194/amt-9-1449-2016, 2016.

Krieger, U. K., Siegrist, F., Marcolli, C., Emanuelsson, E. U., Gøbel, F. M., Bilde, M., Marsh, A., Reid, J. P., Huisman, A. J., Riipinen, I., Hyttinen, N., Myllys, N., Kurtén, T., Bannan, T., Percival, C. J., and Topping, D.: A reference data set for validating vapor pressure measurement techniques: homologous series of polyethylene glycols, Atmos. Meas. Tech., 11, 49–63, https://doi.org/10.5194/amt-11-49-2018, 2017.

Kuang, C., McMurry, P. H., and McCormick, A. V.: Determination of cloud condensation nuclei production from measured new particle formation events, Geophys. Res. Lett., 36, https://doi.org/10.1029/2009gl037584, 2009.

Kulmala, M.: Importance of New Particle Formation for Climate and Air Quality, ACS EST Air, 2, 710–712, https://doi.org/10.1021/acsestair.5c00095, 2025.

Li, H., Almeida, T. G., Luo, Y., Zhao, J., Palm, B. B., Daub, C. D., Huang, W., Mohr, C., Krechmer, J. E., Kurtén, T., and Ehn, M.: Fragmentation inside proton-transfer-reaction-based mass spectrometers limits the detection of ROOR and ROOH peroxides, Atmos. Meas. Tech., 15, 1811–1827, https://doi.org/10.5194/amt-15-1811-2022, 2022.

Li, Y., Pöschl, U., and Shiraiwa, M.: Molecular corridors and parameterizations of volatility in the chemical evolution of organic aerosols, Atmos. Chem. Phys., 16, 3327–3344, https://doi.org/10.5194/acp-16-3327-2016, 2016.

Liu, Y., Attoui, M., Yang, K., Chen, J., Li, Q., and Wang, L.: Size-resolved chemical composition analysis of ions produced by a commercial soft X-ray aerosol neutralizer, J. Aerosol Sci., 147, 105586, https://doi.org/10.1016/j.jaerosci.2020.105586, 2020.

Liu, Y., Attoui, M., Li, Y., Chen, J., Li, Q., and Wang, L.: Characterization of a Kanomax® fast condensation particle counter in the sub-10 nm range, J. Aerosol Sci., 155, 105772, https://doi.org/10.1016/j.jaerosci.2021.105772, 2021.

Lopez-Hilfiker, F. D., Iyer, S., Mohr, C., Lee, B. H., D'Ambro, E. L., Kurtén, T., and Thornton, J. A.: Constraining the sensitivity of iodide adduct chemical ionization mass spectrometry to multifunctional organic molecules using the collision limit and thermodynamic stability of iodide ion adducts, Atmos. Meas. Tech., 9, 1505–1512, https://doi.org/10.5194/amt-9-1505-2016, 2016.

Mohr, C., Thornton, J. A., Heitto, A., Lopez-Hilfiker, F. D., Lutz, A., Riipinen, I., Hong, J., Donahue, N. M., Hallquist, M., Petäjä, T., Kulmala, M., and Yli-Juuti, T.: Molecular identification of organic vapors driving atmospheric nanoparticle growth, Nat. Commun., 10, 4442, https://doi.org/10.1038/s41467-019-12473-2, 2019.

Moller, B., Rarey, J., and Ramjugernath, D.: Estimation of the vapour pressure of non-electrolyte organic compounds via group contributions and group interactions, J. Mol. Liq., 143, 52–63, https://doi.org/10.1016/j.molliq.2008.04.020, 2008.

https://doi.org/10.5194/egusphere-2026-3174
Preprint. Discussion started: 21 July 2026

Nannoolal, Y., Rarey, J., Ramjugernath, D., and Cordes, W.: Estimation of pure component properties Part 1. Estimation of the normal boiling point of non-electrolyte organic compounds via group contributions and group interactions, Fluid Phase Equilibria, 226, 45–63, https://doi.org/10.1016/j.fluid.2004.09.001, 2004.

Qiao, X., Yan, C., Li, X., Guo, Y., Yin, R., Deng, C., Li, C., Nie, W., Wang, M., Cai, R., Huang, D., Wang, Z., Yao, L., Worsnop, D. R., Bianchi, F., Liu, Y., Donahue, N. M., Kulmala, M., and Jiang, J.: Contribution of Atmospheric Oxygenated Organic Compounds to Particle Growth in an Urban Environment, Environ. Sci. Technol., 55, 13646–13656, https://doi.org/10.1021/acs.est.1c02095, 2021.

Ren, S., Yao, L., Wang, Y., Yang, G., Liu, Y., Li, Y., Lu, Y., Wang, L., and Wang, L.: Volatility parameterization of ambient organic aerosols at a rural site of the North China Plain, Atmos. Chem. Phys., 22, 9283–9297, https://doi.org/10.5194/acp-22-9283-2022, 2022.

Riva, M., Rantala, P., Krechmer, J. E., Peräkylä, O., Zhang, Y., Heikkinen, L., Garmash, O., Yan, C., Kulmala, M., Worsnop, D., and Ehn, M.: Evaluating the performance of five different chemical ionization techniques for detecting gaseous oxygenated organic species, Atmos. Meas. Tech., 12, 2403–2421, https://doi.org/10.5194/amt-12-2403-2019, 2019.

Sekimoto, K., Li, S.-M., Yuan, B., Koss, A., Coggon, M., Warneke, C., and Gouw, J. de: Calculation of the sensitivity of proton-transfer-reaction mass spectrometry (PTR-MS) for organic trace gases using molecular properties, Int. J. Mass Spectrom., 421, 71–94, https://doi.org/10.1016/j.ijms.2017.04.006, 2017.

Stolzenburg, D., Fischer, L., Vogel, A. L., Heinritzi, M., Schervish, M., Simon, M., Wagner, A. C., Dada, L., Ahonen, L. R., Amorim, A., Baccarini, A., Bauer, P. S., Baumgartner, B., Bergen, A., Bianchi, F., Breitenlechner, M., Brilke, S., Mazon, S. B., Chen, D., Dias, A., Draper, D. C., Duplissy, J., Haddad, I. E., Finkenzeller, H., Frege, C., Fuchs, C., Garmash, O., Gordon, H., He, X., Helm, J., Hofbauer, V., Hoyle, C. R., Kim, C., Kirkby, J., Kontkanen, J., Kürten, A., Lampilahti, J., Lawler, M., Lehtipalo, K., Leiminger, M., Mai, H., Mathot, S., Mentler, B., Molteni, U., Nie, W., Nieminen, T., Nowak, J. B., Ojdanic, A., Onnela, A., Passananti, M., Petäjä, T., Quéléver, L. L. J., Rissanen, M. P., Sarnela, N., Schallhart, S., Tauber, C., Tomé, A., Wagner, R., Wang, M., Weitz, L., Wimmer, D., Xiao, M., Yan, C., Ye, P., Zha, Q., Baltensperger, U., Curtius, J., Dommen, J., Flagan, R. C., Kulmala, M., Smith, J. N., Worsnop, D. R., Hansel, A., Donahue, N. M., and Winkler, P. M.: Rapid growth of organic aerosol nanoparticles over a wide tropospheric temperature range, Proc. Natl. Acad. Sci. U.S.A, 115, 201807604, https://doi.org/10.1073/pnas.1807604115, 2018.

Stolzenburg, D., Wang, M., Schervish, M., and Donahue, N. M.: Tutorial: Dynamic organic growth modeling with a volatility basis set, J. Aerosol Sci., 166, 106063, https://doi.org/10.1016/j.jaerosci.2022.106063, 2022.

Stolzenburg, D., Sarnela, N., Bianchi, F., Cai, J., Cai, R., Cheng, Y., Dada, L., Donahue, N. M., Grothe, H., Holm, S., Kerminen, V.-M., Lehtipalo, K., Petäjä, T., Sulo, J., Winkler, P. M., Yan, C., Kangasluoma, J., and Kulmala, M.: Incomplete mass closure in atmospheric nanoparticle growth, npj Clim. Atmos. Sci., 8, 75, https://doi.org/10.1038/s41612-025-00893-5, 2025.

Tröstl, J., Chuang, W. K., Gordon, H., Heinritzi, M., Yan, C., Molteni, U., Ahlm, L., Frege, C., Bianchi, F., Wagner, R., Simon, M., Lehtipalo, K., Williamson, C., Craven, J. S., Duplissy, J., Adamov, A., Almeida, J., Bernhammer, A.-K., Breitenlechner, M., Brilke, S., Dias, A., Ehrhart, S., Flagan, R. C., Franchin, A., Fuchs, C., Guida, R., Gysel, M., Hansel, A., Hoyle, C. R.,

https://doi.org/10.5194/egusphere-2026-3174
Preprint. Discussion started: 21 July 2026

Jokinen, T., Junninen, H., Kangasluoma, J., Keskinen, H., Kim, J., Krapf, M., Kürten, A., Laaksonen, A., Lawler, M., Leiminger, M., Mathot, S., Möhler, O., Nieminen, T., Onnela, A., Petäjä, T., Piel, F. M., Miettinen, P., Rissanen, M. P., Rondo, L., Sarnela, N., Schobesberger, S., Sengupta, K., Sipilä, M., Smith, J. N., Steiner, G., Tomè, A., Virtanen, A., Wagner, A. C., Weingartner, E., Wimmer, D., Winkler, P. M., Ye, P., Carslaw, K. S., Curtius, J., Dommen, J., Kirkby, J., Kulmala, M., Riipinen, I., Worsnop, D. R., Donahue, N. M., and Baltensperger, U.: The role of low-volatility organic compounds in initial particle growth in the atmosphere, Nature, 533, 527–531, https://doi.org/10.1038/nature18271, 2016.

Wang, L., Khalizov, A. F., Zheng, J., Xu, W., Ma, Y., Lal, V., and Zhang, R.: Atmospheric nanoparticles formed from heterogeneous reactions of organics, Nat Geosci, 3, 238–242, https://doi.org/10.1038/ngeo778, 2010.

Wang, M., Chen, D., Xiao, M., Ye, Q., Stolzenburg, D., Hofbauer, V., Ye, P., Vogel, A. L., Mauldin, R. L., Amorim, A., Baccarini, A., Baumgartner, B., Brilke, S., Dada, L., Dias, A., Duplissy, J., Finkenzeller, H., Garmash, O., He, X.-C., Hoyle, C. R., Kim, C., Kvashnin, A., Lehtipalo, K., Fischer, L., Molteni, U., Petäjä, T., Pospisilova, V., Quéléver, L. L. J., Rissanen, M., Simon, M., Tauber, C., Tomé, A., Wagner, A. C., Weitz, L., Volkamer, R., Winkler, P. M., Kirkby, J., Worsnop, D. R., Kulmala, M., Baltensperger, U., Dommen, J., El-Haddad, I., and Donahue, N. M.: Photo-oxidation of Aromatic Hydrocarbons Produces Low-Volatility Organic Compounds, Environ. Sci. Technol., 54, 7911–7921, https://doi.org/10.1021/acs.est.0c02100, 2020.

Yang, X., Ren, S., Wang, Y., Yang, G., Li, Y., Li, C., Wang, L., Yao, L., and Wang, L.: Volatility Parametrization of Low-Volatile Components of Ambient Organic Aerosols Based on Molecular Formulas, Environ. Sci. Technol., 57, 11595–11604, https://doi.org/10.1021/acs.est.3c02073, 2023.

Yao, L., Garmash, O., Bianchi, F., Zheng, J., Yan, C., Kontkanen, J., Junninen, H., Mazon, S. B., Ehn, M., Paasonen, P., Sipilä, M., Wang, M., Wang, X., Xiao, S., Chen, H., Lu, Y., Zhang, B., Wang, D., Fu, Q., Geng, F., Li, L., Wang, H., Qiao, L., Yang, X., Chen, J., Kerminen, V.-M., Petäjä, T., Worsnop, D. R., Kulmala, M., and Wang, L.: Atmospheric new particle formation from sulfuric acid and amines in a Chinese megacity, Science, 361, 278–281, https://doi.org/10.1126/science.aao4839, 2018.

Ye, Q., Wang, M., Hofbauer, V., Stolzenburg, D., Chen, D., Schervish, M., Vogel, A., Mauldin, R. L., Baalbaki, R., Brilke, S., Dada, L., Dias, A., Duplissy, J., Haddad, I. E., Finkenzeller, H., Fischer, L., He, X., Kim, C., Kürten, A., Lamkaddam, H., Lee, C. P., Lehtipalo, K., Leiminger, M., Manninen, H. E., Marten, R., Mentler, B., Partoll, E., Petäjä, T., Rissanen, M., Schobesberger, S., Schuchmann, S., Simon, M., Tham, Y. J., Vazquez-Pufleau, M., Wagner, A. C., Wang, Y., Wu, Y., Xiao, M., Baltensperger, U., Curtius, J., Flagan, R., Kirkby, J., Kulmala, M., Volkamer, R., Winkler, P. M., Worsnop, D., and Donahue, N. M.: Molecular Composition and Volatility of Nucleated Particles from α-Pinene Oxidation between −50 °C and +25 °C, Environ. Sci. Technol., 53, 12357–12365, https://doi.org/10.1021/acs.est.9b03265, 2019.

Zhang, X., Li, C., Xue, S., Yang, X., Wang, Y., Li, Y., Cai, R., Yao, L., and Wang, L.: Volatility Parametrization of Atmospheric Organic Compounds Based on Molecular Formula, ACS EST Air, 3, 291–301, https://doi.org/10.1021/acsestair.5c00167, 2026.

https://doi.org/10.5194/egusphere-2026-3174
Preprint. Discussion started: 21 July 2026

Zhang, Y., Wang, Y., Li, C., Li, Y., Yin, S., Claflin, M. S., Lerner, B. M., Worsnop, D., and Wang, L.: Interpretation of mass spectra by a Vocus proton-transfer-reaction mass spectrometer (PTR-MS) at an urban site: insights from gas chromatographic pre-separation, Atmos. Meas. Tech., 18, 3547–3568, https://doi.org/10.5194/amt-18-3547-2025, 2025.